

Imprint of the merger and ring-down on the gravitational wave background from black hole binaries coalescence

S. Marassi,¹ R. Schneider,² G. Corvino,¹ V. Ferrari,¹ and S. Portegies Zwart³

¹*Dipartimento di Fisica 'G. Marconi', Sapienza Università di Roma and Sezione INFN Roma1, Piazzale Aldo Moro 5, Roma, 00185, Italy*

²*INAF, Osservatorio Astronomico di Roma, via di Frascati 33, 00040 Monteporzio Catone, Italy*

³*Leiden Observatory, Leiden University, P.O. Box 9513, 2300 RA Leiden, The Netherlands*

(Received 17 October 2011; published 20 December 2011)

We compute the gravitational wave background (GWB) generated by a cosmological population of black hole-black hole (BH-BH) binaries using hybrid waveforms recently produced by numerical simulations of (BH-BH) coalescence, which include the inspiral, merger, and ring-down contributions. A large sample of binary systems is simulated using the population synthesis code SeBa, and we extract fundamental statistical information on (BH-BH) physical parameters (primary and secondary BH masses, orbital separations and eccentricities, formation, and merger time scales). We then derive the binary birth and merger rates using the theoretical cosmic star formation history obtained from a numerical study which reproduces the available observational data at redshifts $z < 8$. We evaluate the contributions of the inspiral, merger, and ring-down signals to the GWB, and discuss how these depend on the parameters which critically affect the number of coalescing (BH-BH) systems. We find that Advanced LIGO/Virgo have a chance to detect the GWB signal from the inspiral phase with a $(S/N) = 10$ only for the most optimistic model, which predicts the highest local merger rate of $0.85 \text{ Mpc}^{-3} \text{ Myr}^{-1}$. Third generation detectors, such as the Einstein Telescope (ET), could reveal the GWB from the inspiral phase predicted by any of the considered models. In addition, ET could sample the merger phase of the evolution at least for models which predict local merger rates between $[0.053\text{--}0.85] \text{ Mpc}^{-3} \text{ Myr}^{-1}$, which are more than a factor 2 lower than the upper limit inferred from the analysis of the LIGO S5 run [J. Abadie *et al.*, *Phys. Rev. D* **83**, 122005 (2011)]. The frequency dependence and amplitude of the GWB generated during the coalescence is very sensitive to the adopted core mass threshold for BH formation. This opens up the possibility to better understand the final stages of the evolution of massive stellar binaries using observational constraints on the associated gravitational wave emission.

DOI: [10.1103/PhysRevD.84.124037](https://doi.org/10.1103/PhysRevD.84.124037)

PACS numbers: 04.30.Db, 04.25.dg

I. INTRODUCTION

Double black hole binaries are among the most promising sources of gravitational radiation for the ground-based detectors LIGO/Virgo—in their present and advanced configurations which plan to increase the sensitivity by a factor 10 (<http://www.ligo.caltech.edu/>; <http://www.ego-gw.it/>)—and for the future interferometers, the space detector LISA (<http://sci.esa.int/lisa>) and the Einstein telescope [(ET), <http://www.et-gw.eu>]. In addition to the emission from single resolved systems, massive compact binaries generate stochastic backgrounds of gravitational waves (GWB), as extensively discussed in the literature [1–8]. If detected, these backgrounds would provide information on the cosmic star formation history, on the evolution of compact stars in binary systems, and on cosmological parameters [9,10]; even if these signals were not detected, more stringent upper limits would rule out the most optimistic theoretical models. Astrophysical backgrounds act as a confusion-limited foreground noise for signals generated in the early Universe (primordial GWBs); therefore, the spectral properties which characterize the background generated by

various families of compact binaries need to be accurately modeled, and specific techniques need to be envisaged in order to disentangle their contribution from the instrumental noise [11–13].

The aim of the present work is to provide updated estimates of the GWB generated by a cosmological population of black hole-black hole (BH-BH) binaries, including the contribution due to the merging of the two bodies, and to the ring-down of the final black hole. The full signal is modeled using the waveforms derived in [14]; they combine the inspiral part of the signal (obtained with the standard post-Newtonian description) and the ring-down oscillations of the final black hole, with the signal emitted during the merging phase, whose description has been made possible by recent progresses in numerical relativity. We will show that, since a significant amount of energy is radiated during the merger and ring-down, these phases give a significant contribution to the produced background.

A recent estimate of GWB from coalescing black hole binaries using the same waveforms has been presented in [7]. This study adopts average quantities for the single source emission and a fixed distribution for the delay between the birth of a binary and its merging (merger

time scale); furthermore, they normalize the (BH-BH) merger rate to a “local value” inferred from models of Galactic binary populations.

Here we follow a different approach. We use the population synthesis code SeBa [15] (<http://www.sns.ias.edu/~starlab/>) to simulate the properties of a large sample of double black hole binaries. This enables us to investigate the statistical distributions of masses and merger time scales in a self-consistent way. Following [16,17], we adopt a theoretical model for the cosmic star formation history at redshifts $z < 20$ taken from the numerical simulation of [18], which reproduces the observational data available at $z < 8$ [19]. With these inputs, we compute the redshift evolution of the (BH-BH) birth and merger rates and the cumulative gravitational wave signal produced throughout the Universe. We stress the contributions of the inspiral, merger, and ring-down phases of the coalescence process to the total background, and discuss their detectability.

Finally, we run a set of independent SeBa simulations to single out the parameters which critically affect the number of coalescing (BH-BH) systems, the GWB, and its detectability; we find these to be the common envelope parameter, the core mass threshold for BH formation, and the kick velocity distribution.

As first noted in [20], close black hole binaries form efficiently through dynamical interactions in dense globular clusters or in nuclear star clusters [21–23]. However, in the present analysis we do not consider this additional formation channel, since it requires a different modeling which is not included in the current version of SeBa.

The plan of the paper is the following. In Sec. II we briefly describe the SeBa code and the underlying physical assumptions which we use to simulate the sample of (BH-BH) binaries. A statistical analysis of the resulting population is presented in Sec. III. In Sec. IV we outline the main features of the waveforms we adopt to describe the gravitational emission of (BH-BH) binaries and in Sec. V we compute, starting from the cosmic star formation history, the evolution of the birth and merger rates of (BH-BH) binaries. In Sec. VI, we present the resulting density parameter of the GWB, Ω_{GW} , we discuss its detectability by second and third generations interferometric detectors, and its dependence on key physical parameters. Finally, in Sec. VII we draw our conclusions.

II. SEBA POPULATION SYNTHESIS CODE

To compute the statistical properties of a black hole binary population, we use the latest release of the population synthesis code SeBa [15], which is based on previous versions described in [3,24–26].

In SeBa, the evolution of binary systems is modeled by taking into account the relevant physics, which include stellar composition, stellar wind, mass transfer and accretion, gravitational radiation, magnetic braking, common

envelope phase, and supernovae (for more details see the original papers). The present version of the code uses updated stellar and binary physics, including results from supernova simulations [27]. In particular, new features about the evolution of massive stars, Wolf-Rayet stars, stellar wind mass-loss rate, common envelope phase, fallback prescription, and supernova kicks are discussed in detail in [15]. The predictions of the code have been tested against observational data on double neutron star binaries [25], BH-candidate short-period binaries [15], type II and Ib/c SNe [3,26], and more recently, SN type Ia [28]. Here we sketch a summary of the assumptions that are relevant for the evolution of (BH-BH) binaries.

For the common envelope evolution (CE), we use the standard prescription described in [3,29,30], with the efficiency and the structure parameters α_{CE} and λ combined into a single quantity, $\alpha_{\text{CE}} \times \lambda$. The treatment of the common envelope evolution is still under debate; at present, a strict criterion to define the binding energy of the stellar envelope is still lacking and it is unclear whether other sources of energy, beyond gravitational energy, contribute to unbind the common envelope ([31–36] and references therein). As a result, $\alpha_{\text{CE}} \times \lambda$ is a free parameter of population synthesis models. For our reference model A (see Sec. III), we fix $\alpha_{\text{CE}} \times \lambda = 2$, chosen so as to reproduce the available observational constraints [37], such as the neutron star-neutron star (NS-NS) merger rate inferred from double pulsar observations [38,39].

As suggested in [40–42], black holes receive a small asymmetric kick at birth: in our reference simulation (model A) this kick is taken from a Paczyński velocity distribution [43,44], isotropic in space and scaled down with the ratio of black hole to neutron star masses (see Table I).

Black hole formation is treated in the code assuming that a constant fraction of the supernova explosion energy is used to unbind the stellar envelope [27]; we choose $f = 0.4$. However, while in [27] the explosion energy is assumed to be a function of the presupernova mass, we keep it fixed at 10^{50} erg. This value is within the expected range, but favors the formation of rather massive black holes (up to $15M_{\odot}$, see also [15]).

Regarding the evolution of massive ($15M_{\odot} \leq M_i \leq 85M_{\odot}$) stars, SeBa assumes that stellar wind mass-loss rate increases in time; in their total lifetime, stars lose an amount of matter which is a function of their initial mass, $0.01M_i^2$; the hydrogen envelope is lost when the stars are still on the main sequence. For higher masses ($M_i > 85M_{\odot}$) the mass-loss rate is very uncertain: we assume that, during the main sequence lifetime, these stars lose $43M_{\odot}$. Because of the paucity of these massive stars, this crude assumption has negligible consequences on the estimate of the GWB.

When the star loses its hydrogen envelope on the main sequence, stellar mass-loss prescription for Wolf-Rayet

TABLE I. Zero-age parameters for the reference model A (see text).

Model A Parameter	Symbol	Value	Note
Mass of primary star	M_{prim}	$[8-100]M_{\odot}$	Salpeter IMF (-2.35)
Mass of the secondary star	M_{sec}	$M_{\text{sec}} = qM_{\text{prim}}$	The distribution matches the q distribution
Mass ratio	q	$[0-1]$	Flat distribution
Initial semimajor axis	sma	$0.1-10^6 R_{\odot}$	Flat distribution in $\log \text{sma}$
Eccentricity	e	$[0-1]$	Thermal equilibrium distribution
CE parameter	$\alpha_{\text{CE}}\lambda$	2	Structure parameter
Kick distribution for NS	$u = v/\sigma$	$\sigma = 300 \text{ km s}^{-1}$	Paczynski distribution for v
Kick distribution for BH	v_{BH}	-	Same as NS but scaled down: $v_{\text{BH}} = v(M_{\text{NS}}/M_{\text{BH}})$
Core mass threshold	$m_{\text{thre, BH}}$	$10M_{\odot}$	[15]

stars is adopted. More details on the treatment of massive stars in the code are described in [15] (see, in particular, Sec. 2.3 and Fig. 1). For Wolf-Rayet stars the mass-loss rate by [45] is adopted, which is based on the compilation of mass-loss rates inferred from observations of Wolf-Rayet stars [46].

We initialize $N = 10^6$ “zero-age” binaries (ZAMS). The zero-age parameters of the simulated population are given in Table I for our reference model A. These are randomly selected from a set of independent distribution functions. In particular, the initial primary mass M_{prim} is taken from a Salpeter initial mass function (IMF), $\Phi(M) \propto M^{-(1+x)}$ with $x = 1.35$, between $[8-100]M_{\odot}$; the initial secondary mass, M_{sec} , is selected from a flat distribution for the mass ratio $q = M_{\text{sec}}/M_{\text{prim}}$. The semimajor axis (sma) distribution is flat in $\log(\text{sma})$ [47] ranging from $0.1R_{\odot}$ (Roche lobe contact) up to 10^6R_{\odot} . We assume a thermal eccentricity distribution $\Phi(e) = 2e$ in the range

$[0-1]$ [48]. Kicks follow a Paczynski velocity distribution with a dispersion of $\sigma = 300 \text{ km s}^{-1}$ [43].

We have explored a wide parameter space to investigate how different choices affect the resulting GWB. This has enabled us to identify the physical parameters which have the largest impact on the GWB, and the corresponding models will be presented in Sec. VI B.

Finally, we note that the version of SeBa that we use assumes an initial solar metallicity for all stars.

III. STATISTICAL PROPERTIES OF BLACK HOLE BINARIES POPULATION

In this section, we present the statistical properties of (BH-BH) binaries and their progenitors for our reference model A (see Table I). A great uncertainty in the modeling of black hole binaries is due to our poor knowledge of the BH mass distribution and its relation to the initial distribution of progenitor masses. The upper mass limit of isolated stars for black hole formation depends predominantly on wind mass loss; recent studies constrain the mass range of black hole progenitors to $M \sim [20-60]M_{\odot}$ [27,37,49,50]. Clearly, a massive progenitor in a binary system might follow a different evolutionary path which would affect the mass of the nascent black hole [27,45,51,52].

Figure 1 shows the mass range of primary and secondary progenitors of (BH-BH) systems (empty grey circles). Black squares show the subsample of progenitors which generate (BH-BH) binaries with merger times smaller than the Hubble time ($t_{\text{H}} \sim 13.4 \text{ Gyr}$ for our adopted cosmological model [53]). Primary (secondary) progenitors have masses in the range $30M_{\odot} \leq M_{\text{prim}} \leq 100M_{\odot}$ ($20M_{\odot} \leq M_{\text{sec}} \leq 100M_{\odot}$). Merging systems come from a narrower dynamical range, with 90% (96%) having primary (secondary) progenitor mass $30M_{\odot} \leq M_{\text{prim}} \leq 60M_{\odot}$ ($20M_{\odot} \leq M_{\text{sec}} \leq 50M_{\odot}$).

Observations of BH candidates in binary systems suggest a range of masses in the $[4-17]M_{\odot}$ interval ([37,54,55] and references therein), in broad agreement with theoretical simulations, which indicate a range of black hole

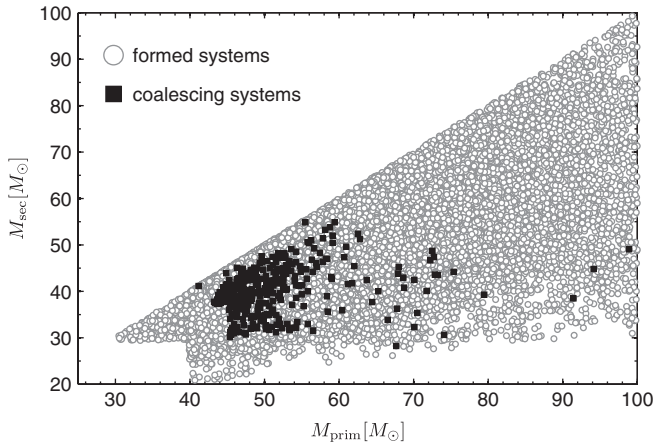


FIG. 1. Mass of the secondary stellar progenitors as a function of the corresponding primary mass. Empty grey circles indicate stellar binaries which lead to (BH-BH) systems; black squares show the subsample of these progenitors which form (BH-BH) binaries with merger times smaller than the Hubble time (see text).

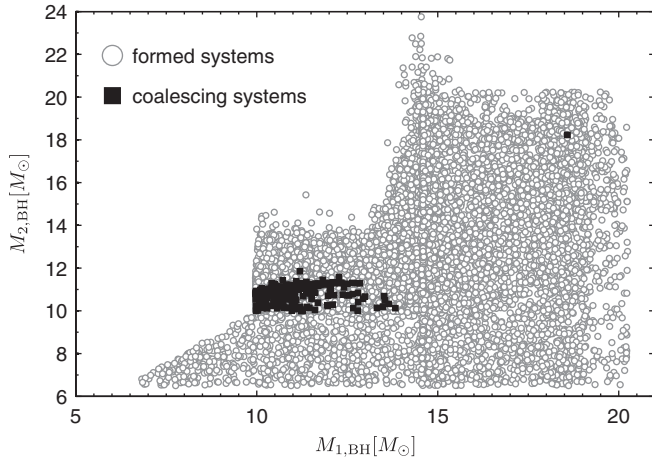


FIG. 2. Same as Fig. 1 but for black hole primary and secondary masses. The various regions in the parameter space which are overpopulated or underpopulated originate from the decision making process in SeBa, and can be related to the chain of events in the population synthesis.

masses up to $[10-15]M_{\odot}$ [27,52]. In Fig. 2 we plot the primary and secondary black hole masses, $M_{1,BH}$ and $M_{2,BH}$ (black squares) for model A. Primary and secondary black holes have comparable masses, ranging between $\sim 6M_{\odot}$ up to $\sim 20M_{\odot}$; these limits are consistent with the observational and theoretical estimates quoted above.

Merging pairs are concentrated in a narrow range of masses, with the primary BH mass in the range $[10-15]M_{\odot}$ and the secondary in the range $[10-11]M_{\odot}$. This corresponds to a BH mass ratio, q_{BH} , in the range $[1-1.1]$ (see also Fig. 4), where q_{BH} is defined as the ratio of the heaviest to the lightest BH mass.

In the upper panel of Fig. 3, we show the time interval from the formation of the ZAMS binary system to the formation of the compact black hole binary, τ_s ; we plot this quantity as a function of the semimajor axis, sma , showing only those systems with $sma < 1600R_{\odot}$, which represent $\sim 60\%$ of the total. The formation time of compact binaries is very small, ranging between ~ 3.5 to ~ 6 Myr. Black squares indicate merging black hole binaries, which are those that, at the time of their formation, have semimajor axes smaller than $20R_{\odot}$, comparable to that found in [56] (see their Fig. 2).

It is important to note that only 2% of (BH-BH) pairs is able to reach the final coalescence. Figure 3 shows that the majority of (BH-BH) systems is characterized by large orbital separations (and periods). In fact, progenitors with masses $\geq 40M_{\odot}$ experience large mass-loss rates which remove mass from the binary increasing the orbital separation.

Once compact degenerate binaries are formed, the emission of gravitational radiation is the only physical process driving the change in orbital parameters. In the lower panel of Fig. 3, we show the merger time as a function of the chirp mass, defined as

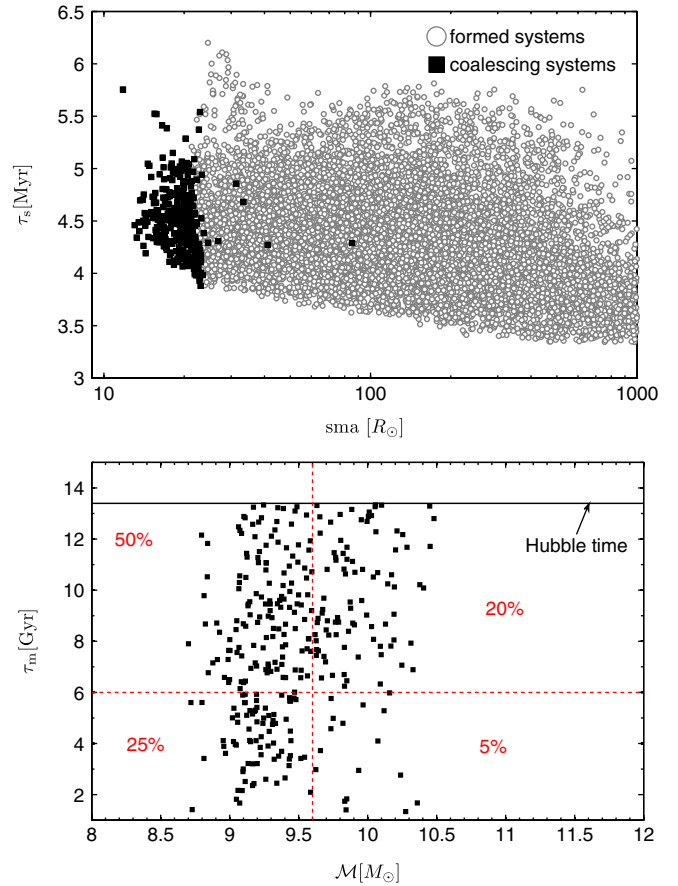


FIG. 3 (color online). Upper panel: Formation time scales for compact black hole binaries as a function of the corresponding semimajor axis. For clarity, only systems with $sma < 1600R_{\odot}$ are shown (empty grey circles). Black squares are (BH-BH) pairs with merger times smaller than the Hubble time (see text). Lower panel: Merger time scales as a function of the chirp mass of merging systems. The dashed horizontal and vertical lines indicate threshold values, $\tau_{m,thre}$ and \mathcal{M}_{thre} , so that 70% of the systems have $\tau_m > \tau_{m,thre}$ and 75% have $\mathcal{M} < \mathcal{M}_{thre}$.

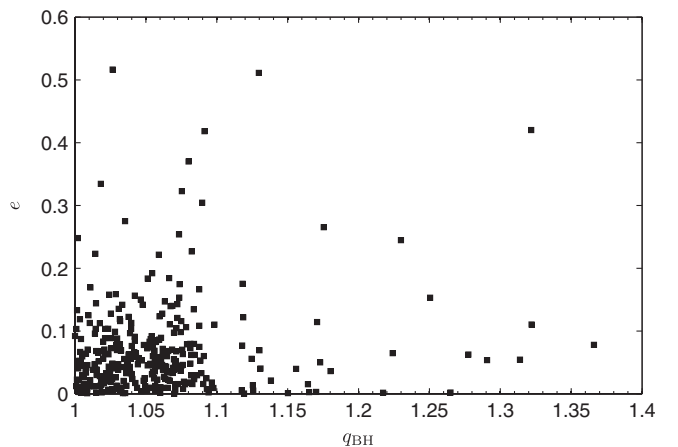


FIG. 4. Eccentricity as a function of the black hole mass ratio for merging systems.

$$\mathcal{M} = \mu^{3/5} M^{2/5},$$

where $\mu = M_{1,\text{BH}}M_{2,\text{BH}}/M$ and $M = M_{1,\text{BH}} + M_{2,\text{BH}}$ are the reduced and total mass, respectively. It is clear from the figure that all merging pairs have relatively long merger times, $\tau_m > 1$ Gyr and 70% have $\tau_m > 6$ Gyr (horizontal dashed line); the chirp masses lie in the interval $[8.5\text{--}10.5]M_\odot$ and 75% of the systems have $\mathcal{M} < 9.6M_\odot$ (vertical dashed line). Although the plot does not show any clear correlation between τ_m and \mathcal{M} , half of the systems lie in the upper left region and only 5% in the bottom right.

Finally, in Fig. 4 we show the distribution of orbital eccentricity as a function of the black hole mass ratio for merging pairs at the time of formation of the compact binary systems. The inspiral part of the adopted waveform depends on the BH masses and it is strictly applicable only to (BH-BH) binaries in quasicircular orbit. From Fig. 4 we see that only 10% of the systems have $e > 0.15$. Furthermore, using the relation between the orbital separation and the eccentricity due to gravitational wave emission [57,58], we find that by the time (BH-BH) binaries enter the Advanced LIGO and ET bands (10 and 1 Hz, respectively), the eccentricities are smaller than 10^{-4} for all systems, and consequently the assumption of quasicircular orbits is well justified.

IV. BLACK HOLE BINARIES AS GW SOURCES

To evaluate the background produced by a cosmological population of coalescing (BH-BH) binaries, we use the family of waveforms obtained in [14], which model the inspiral, merger, and ring-down phases for the coalescence of nonspinning black holes. These waveforms refer to the leading harmonic of the gravitational signal ($\ell = 2$, $m = \pm 2$), which is the dominant contribution for low mass ratios ($q_{\text{BH}} \sim 1$). In the frequency domain, the signal has the form

$$h(f) = A_{\text{eff}}(f)e^{i\Psi_{\text{eff}}(f)}, \quad (1)$$

where f is the emission frequency. The wave amplitude is given by

$$A_{\text{eff}}(f) = C \begin{cases} \left(\frac{f}{f_{\text{merg}}}\right)^{-7/6} & \text{if } f < f_{\text{merg}} \\ \left(\frac{f}{f_{\text{merg}}}\right)^{-2/3} & \text{if } f_{\text{merg}} < f < f_{\text{ring}} \\ w\mathcal{L} & \text{if } f_{\text{ring}} < f < f_{\text{cut}}, \end{cases} \quad (2)$$

where the constants ($f_{\text{merg}}, f_{\text{ring}}, f_{\text{cut}}$), which identify the frequency regions where the emitting system is inspiraling, merging, and oscillating, are

TABLE II. Values of the constants which appear in the wave amplitude [Eq. (2)] taken from [14].

k	a_k	b_k	c_k
0	6.6389×10^{-1}	-1.0321×10^{-1}	1.0979×10^{-1}
1	1.3278	-2.0642×10^{-1}	2.1957×10^{-1}
2	1.1383	-1.7700×10^{-1}	4.6834×10^{-2}
3	1.7086	-2.6592×10^{-1}	2.8236×10^{-1}

$$\begin{aligned} f_{\text{merg}} &= \frac{a_0\eta^2 + b_0\eta + c_0}{\pi M}, \\ f_{\text{ring}} &= \frac{a_1\eta^2 + b_1\eta + c_1}{\pi M}, \\ f_{\text{cut}} &= \frac{a_3\eta^2 + b_3\eta + c_3}{\pi M}. \end{aligned} \quad (3)$$

In these expressions $\eta = M_{1,\text{BH}}M_{2,\text{BH}}/M^2$ is the symmetric mass ratio, and the coefficients a_k, b_k , and c_k (with $k = 0, 1, 2, 3$) are given in Table II. The constants C and w , and the function \mathcal{L} , which characterize the wave amplitude, are

$$\begin{aligned} C &= \frac{M^{5/6}}{d\pi^{2/3}f_{\text{merg}}^{7/6}} \left(\frac{5\eta}{24}\right)^{1/2}, \\ w &= \frac{\pi\sigma}{2} \left(\frac{f_{\text{ring}}}{f_{\text{merg}}}\right)^{-2/3}, \\ \mathcal{L} &= \left(\frac{1}{2\pi}\right) \frac{\sigma}{(f - f_{\text{ring}})^2 + \sigma^2/4}, \end{aligned} \quad (4)$$

where $\sigma = (a_2\eta^2 + b_2\eta + c_2)/\pi M$. We do not need to compute the phase of the signal since the single source GW spectrum depends on the squared GW amplitude [see Eq. (11)]. The model assumes optimal orientation of the detector with respect to the emitting source.

In Fig. 5 we plot the dimensionless amplitude $fh(f)$ as a function of frequency, for a system with total mass $M = 20M_\odot$, symmetric mass ratio $\eta = 0.25$, located at a distance of 10 Mpc. The frequency limits, which identify the

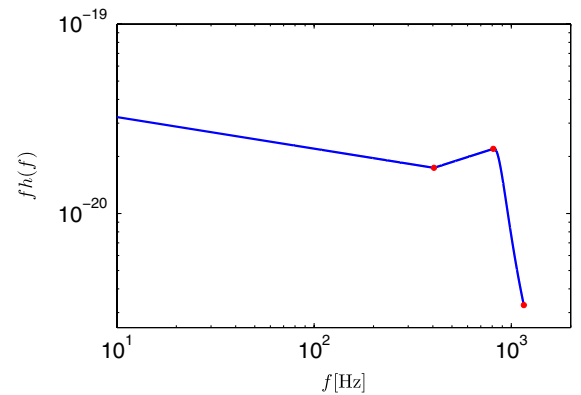


FIG. 5 (color online). Single source signal as a function of frequency for a (BH-BH) binary with total mass $M = 20M_\odot$, symmetric mass ratio $\eta = 0.25$, located at a distance of 10 Mpc.

three regimes (inspiral, merger, and ring-down), are $f_{\text{merg}} = 405$ Hz, $f_{\text{ring}} = 810$ Hz, and $f_{\text{cut}} = 1042$ Hz (points on the curve). These frequencies are inversely proportional to the total mass of the binary. Hence, for the most massive binaries in the simulated sample, with $M = 40M_{\odot}$ (see Fig. 2), f_{merg} , f_{ring} , and f_{cut} are a factor of 2 smaller than the values plotted in the figure.

V. FROM STAR FORMATION TO BINARY FORMATION RATE

In this section we derive the evolution of the birth rate of binary systems from the comoving star formation rate density as a function of redshift, inferred from the simulations in [18]. These cosmological simulations are characterized by an improved treatment of metal enrichment and the stellar IMF is assigned depending on the gas metallicity. In particular, population II/I stars form in the mass range $[0.1-100]M_{\odot}$ according to a Salpeter IMF in regions which have been already polluted by the first metals and dust grains to a metallicity $Z > Z_{\text{cr}} = [10^{-6} - 10^{-4}]Z_{\odot}$ [59–61]. Below this threshold, gas cooling is inefficient and the star formation process favors the formation of very massive (population III) stars, characterized by a top-heavy IMF (for more details on the numerical scheme we refer to [18]). In this work, we are only interested in population II/I stellar progenitors of black holes.

Starting from the star formation rate density at a given z , $\dot{\rho}_{\star}(z)$ (expressed in units of $M_{\odot} \text{ yr}^{-1} \text{ Mpc}^{-3}$), we derive the binary birth rate per comoving volume (expressed in units of $\text{yr}^{-1} \text{ Mpc}^{-3}$) as

$$\dot{R}_{\text{bin}}(z) = \frac{dR}{dt dV}(z) = \frac{\dot{\rho}_{\star}(z)}{\langle m_{\star} \rangle} \times \frac{f_{\text{bin}}}{2} \times f_{\text{sim}}, \quad (5)$$

where f_{bin} is the binarity fraction (which we take to be 1), $\langle m_{\star} \rangle$ is the average stellar mass, and f_{sim} is the fraction of binaries simulated by the population synthesis code SeBa. The latter quantity accounts for the fact that, while in the original simulation of [18] stars are assumed to have masses in the range $[0.1-100]M_{\odot}$, in SeBa we initialize only binary systems with primary mass in the range $[8-100]M_{\odot}$, in order to increase the statistics on double (BH-BH) binaries. Thus, the fraction of simulated systems is

$$f_{\text{sim}} = \frac{\int_8^{100} dM_{\text{prim}} \Phi(M_{\text{prim}})}{\int_{0.1}^{100} dM_{\text{prim}} \Phi(M_{\text{prim}})}, \quad (6)$$

and the average stellar mass is

$$\langle m_{\star} \rangle = \frac{\int_{0.1}^{100} dM_{\text{prim}} M_{\text{prim}} \Phi(M_{\text{prim}})}{\int_{0.1}^{100} dM_{\text{prim}} \Phi(M_{\text{prim}})}. \quad (7)$$

Following [1], we assume that a ZAMS binary forms at a redshift z_s ; after a time interval τ_s the system has evolved into a (BH-BH) binary. Consequently, the redshift of formation of the degenerate binary system, z_f is defined

through $t(z_f) = t(z_s) + \tau_s$. Once the (BH-BH) binary system is formed, it evolves according to gravitational wave emission until, after a time interval τ_m , it eventually coalesces. The redshift z_c at which coalescence occurs is defined by $t(z_c) = t(z_f) + \tau_m$. The number of (BH-BH) systems formed per unit time and comoving volume at redshift z_f is

$$\dot{R}_{(\text{BH-BH})}^{\text{birth}}(z_f) = \int d\tau_m \int_0^{t(z_f)-t(z_F)} d\tau_s \frac{N_{(\text{BH-BH})}}{N} \times \frac{\dot{R}_{\text{bin}}(z_s)}{(1+z_s)} p_{(\text{BH-BH})}(\tau_s, \tau_m), \quad (8)$$

where z_F defines the onset of star formation ($z_F \sim 20$ in the simulation), $N_{(\text{BH-BH})}$ is the number of (BH-BH) systems, N is the total number of simulated binaries, and $p_{(\text{BH-BH})}(\tau_s, \tau_m)$ is the joint probability distribution of delay times. Similarly, the number of (BH-BH) systems per unit time and comoving volume which merge at redshift z_c is

$$\dot{R}_{(\text{BH-BH})}^{\text{merger}}(z_c) = \int_0^{t(z_c)-t(z_F)} d\tau_m \int_0^{t(z_c)-\tau_m-t(z_F)} d\tau_s \frac{N_{(\text{BH-BH})}}{N} \times \frac{\dot{R}_{\text{bin}}(z_s)}{(1+z_s)} p_{(\text{BH-BH})}(\tau_s, \tau_m). \quad (9)$$

In Fig. 6 we show the redshift evolution of the binary birth rate (solid line). Of all these systems, only 1.7% form a (BH-BH) binary. The evolution of the (BH-BH) birth and merger rates is also shown in the figure (dashed and dotted lines, respectively). Since τ_s is relatively short (less than ~ 6 Myr), the evolution of $\dot{R}_{(\text{BH-BH})}^{\text{birth}}$ is simply a scaled-down version of \dot{R}_{bin} . Conversely, there is a shift in the evolution of $\dot{R}_{(\text{BH-BH})}^{\text{merger}}$ which is due to the long merger time scales, $\tau_m > [1-5]$ Gyr.

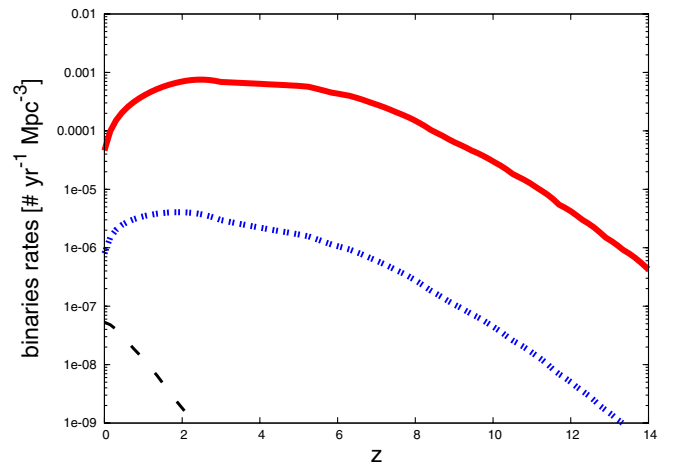


FIG. 6 (color online). Redshift evolution of the total binary birth rate (solid red line) and of (BH-BH) birth and merger rates (dotted and dashed, respectively).

TABLE III. Galactic birth/merger rates obtained from the simulation of model A normalizing to a Galactic supernova rate of $1 \times 10^{-2} \text{ yr}^{-1}$ (see text).

Galactic birth/merger rates		
Type	Birth rates (yr^{-1})	Merger Rates (yr^{-1})
(NS-NS)	8.2×10^{-5}	2.0×10^{-5}
(BH-NS)	5.3×10^{-5}	6.2×10^{-6}
(BH-BH)	9.5×10^{-5}	1.8×10^{-6}

For the sake of comparison, we calculate the Galactic birth and merger rates for (BH-BH), (BH-NS), and (NS-NS) systems extracted from the simulation of model A. To compute these rates, we normalize the total number of core-collapse SNe that we find in the simulation to an estimated Galactic supernova rate of $1 \times 10^{-2} \text{ yr}^{-1}$ [62]. The resulting values are presented in Table III and are in good agreement with the current literature on the subject (see [3,4,25,37,63] and references therein).

VI. GWB FROM BLACK HOLE BINARIES

Following [1,16], we write the spectral energy density of the GWB produced by a population of (BH-BH) binaries as

$$\frac{dE}{dSdfdt} = \int_0^{z_F} d\dot{N}_{(\text{BH-BH})}^{\text{birth}} \left\langle \frac{dE}{dSdf} \right\rangle, \quad (10)$$

where $d\dot{N}_{(\text{BH-BH})}^{\text{birth}} = \dot{K}_{(\text{BH-BH})}^{\text{birth}} \frac{dV}{dz} dz$ and the locally measured average GW energy flux from a single source at redshift z is

$$\left\langle \frac{dE}{dSdf} \right\rangle = \frac{c^3}{G} \frac{\pi}{2} f^2 (1+z)^2 |h[f(1+z)]|^2. \quad (11)$$

Here $f = f_e(1+z)^{-1}$ is the redshifted emission frequency and h is the amplitude of the GW signal given in Eq. (1). The GWB is conventionally characterized by the dimensionless quantity $\Omega_{\text{GW}}(f) \equiv \rho_{\text{cr}}^{-1} (d\rho_{\text{gw}}/d\log f)$, which is related to the spectral energy density by the equation

$$\Omega_{\text{GW}}(f) = \frac{f}{c^3 \rho_{\text{cr}}} \left[\frac{dE}{dSdfdt} \right], \quad (12)$$

where $\rho_{\text{cr}} = 3H_0^2/8\pi G$ is the cosmic critical density.

In Fig. 7 we plot Ω_{GW} , as a function of the observational frequency, for the reference model A. The cumulative signal is the result of the emission during the inspiral (dashed line), merger (solid line), and ring-down (dotted line) phases of the coalescence processes. In the frequency range $10 \text{ Hz} \lesssim f \lesssim 200 \text{ Hz}$, the signal is dominated by the inspiral phase which reaches a maximum amplitude of $\Omega_{\text{GW}} = 7.8 \times 10^{-10}$ at a frequency of $\sim 200 \text{ Hz}$. Above this limit, a further increase in the signal is driven by the emission during the merger phase, which reaches a maximum $\Omega_{\text{GW}} = 2.1 \times 10^{-9}$ at 540 Hz . This is not surprising,

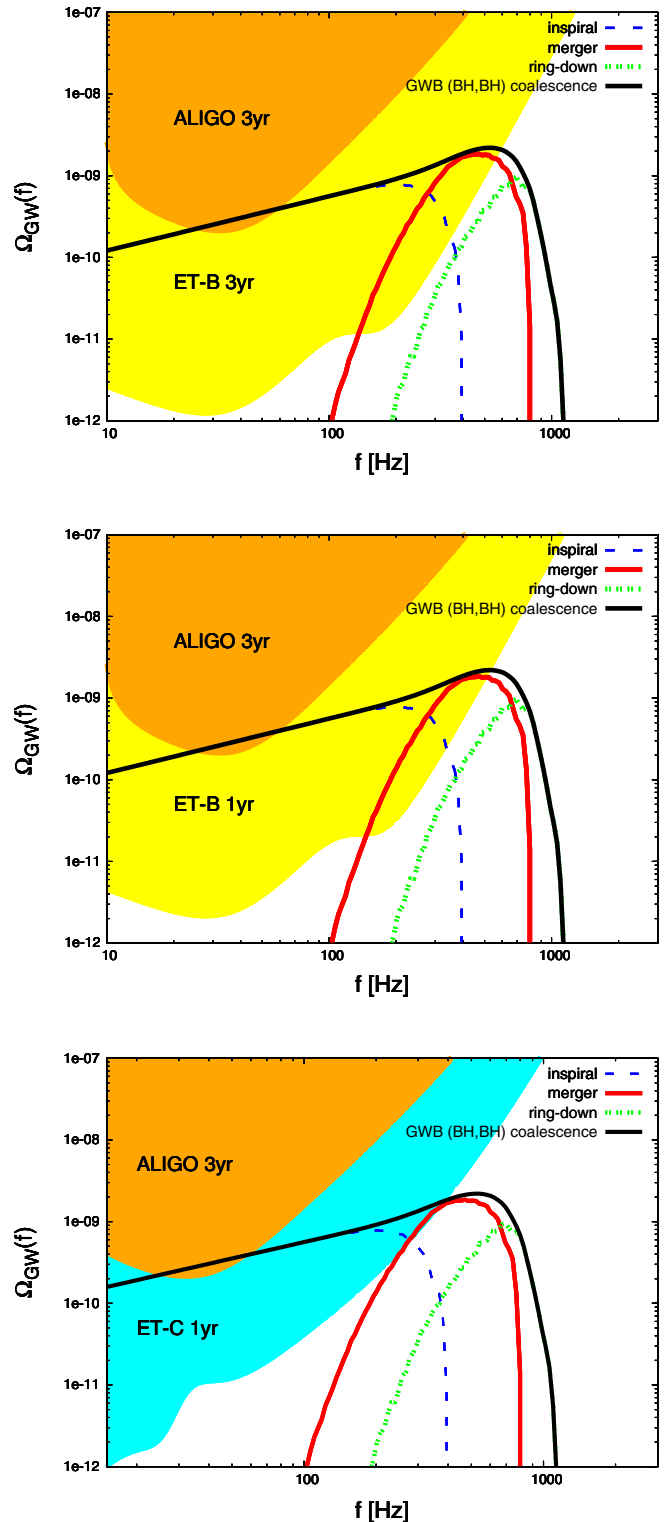


FIG. 7 (color online). The closure energy density, Ω_{GW} , generated by (BH-BH) coalescing binaries in model A, plotted as a function of the observational frequency. The three contributions coming from the inspiral (dashed), merger (solid), and ring-down (dotted) phases are plotted separately. The black solid line is the total GWB signal. The shaded regions in the three panels indicate the foreseen sensitivities for different interferometers and integration times (see labels on the figures).

since a significant portion of GW energy is radiated during the merger. At larger frequencies, the signal drops with a minor contribution coming from the ring-down phase which follows the final coalescence of the two black holes in each binary.

In Fig. 7, the GWB signal is compared with the foreseen sensitivity curves for advanced LIGO/Virgo (ALIGO) and for the Einstein telescope with two different design configurations (ET-B and ET-C) and assuming 1 yr or 3 yrs of integration time. In particular, ALIGO with 3 yrs of integration might sample only a small portion of the inspiral phase with (S/N) ratios below the detection threshold (see Sec. VIA). The full inspiral and merger phases might be observed with ET, even with an integration time of one year. The best configuration appears to be ET-B (see discussion below) which amplifies the sensitivity at larger frequencies. In Sec. VIA, we estimate the detectability of the signal in a quantitative way and in Sec. VIB we discuss the dependence of the GWB and of its detectability on some key physical parameters.

A. Detectability

We consider the design sensitivities of second generation interferometric detectors, Advanced LIGO/Virgo, [64] in a configuration of zero detuning of the signal recycling mirror, with high laser power. For the third generation interferometer ET, we consider two target sensitivities. The first configuration, ET-B, is an underground based design, incorporating long suspension, cryogenics, and signal power recycling. The second configuration, ET-C, is called *Xylophone* configuration and merges the output of two detectors specialized in different frequency bands (for more details see [65,66]).

It is known that the detection strategy for continuous GWB signals is to cross correlate the output of two detectors that are assumed to be sufficiently well separated that their noise sources are largely uncorrelated [67].

The statistical nature of the background depends on the duration of the signal, on the event rate and on the lower frequency bound of the detector, f_L , the so-called “seismic wall” (see for a discussion [68]).

Assuming that for ALIGO $f_L = 10$ Hz, the background predicted for the reference model A would be characterized by a duty cycle of $\sim 5 \times 10^{-3}$. For ET, which has a lower $f_L = 1$ Hz, the duty cycle would be ~ 2 . According to [69], the cross-correlation method is found to be nearly optimal for duty cycles $> 10^{-3}$. Therefore, in what follows we estimate the detectability of the signal using this method, as in [7], and we do not distinguish between the resolvable and the nonresolvable components [70]. We use the cross-correlation statistics to calculate the optimized S/N for an integration time T as given by [11],

$$\left(\frac{S}{N}\right)^2 \approx \frac{9H_0^4}{50\pi^4} T \int_0^\infty df \frac{\gamma^2(f) \Omega_{\text{GW}}^2(f)}{f^6 P_1(f) P_2(f)}, \quad (13)$$

where $P_1(f)$ and $P_2(f)$ are the power spectral noise densities of the two detectors and γ is the normalized overlap reduction function, which quantifies the loss of sensitivity due to the separation and the relative orientation of the detectors.

We have computed the (S/N) ratio assuming different integration times (1–3 years) and detector separation/orientation (case-I and case-II). For ALIGO, case-I considers the LIGO Hanford/Livingston pair using γ in the form given by Eq. (3.26) in [71]. For ET-B and ET-C, case-I adopts the constant value $\gamma = -3/8$ which applies to two ET detectors operating in the frequency range [1–1000] Hz [65]. Case-II is the same for all detectors and represents a pair of aligned equivalent detectors situated within several km. This optimal case corresponds to $\gamma = 1$.

The resulting (S/N) ratios are reported in Table IV. The values refer to model A (see Table I), and are obtained assuming a threshold signal-to-noise ratio of 3 which corresponds to a false alarm rate of 10% and to a detection rate of 90% [for more details, see Eq. (19) in [17]].

The highest (S/N) ratios are obtained with optimal orientation (case-II) and longer integration times. These conditions would not allow ALIGO to detect the coalescence signal. The increase in sensitivity foreseen for ET would enable the detectability of two portions of the signal, the inspiral and the merger phases, with $(S/N) > 5$,

TABLE IV. The (S/N) ratio for second and third generation detectors, assuming different integration times and detector separation/orientation (see text). The values refer to model A (see Table I) and have been computed considering the cumulative signal (coalescence) and separate contributions from the inspiral, merger, and ring-down phases.

(S/N)				
Case II [Case I]				
GWB	ALIGO (3 yr)	ET-B (3 yr)	ET-B (1 yr)	ET-C (1 yr)
Coalescence	1.9 [0.7]	316 [118]	182 [68]	275 [103]
Inspiral	1.9 [0.7]	310 [116]	179 [67]	274 [103]
Merger	7.5×10^{-2} [6.4×10^{-4}]	26 [9]	15 [5.6]	5 [1.9]
Ring-down	8.1×10^{-3} [3.3×10^{-5}]	1.5 [0.6]	0.9 [0.3]	0.4 [0.1]

independently of the adopted separation/orientation and integration times.

B. Dependence on physical parameters

In this section we analyze the dependence of the GWB on some key physical parameters that affect the (BH-BH) birth/merger rates, i.e. the adopted kick velocity distribution, the CE parameter, and core mass threshold for black hole formation, $m_{\text{thre, BH}}$.

In Table V we list a set of models (first column) which differ from the reference model A by the variation of a single parameter, indicated in the second column. For each model, in columns 3 and 4 we tabulate the Galactic (BH-BH) birth and merger rates. Similarly to that done in Sec. V (Table III), these values are obtained by normalizing the supernova rate predicted by each SeBa run to the Galactic rate of $1 \times 10^{-2} \text{ yr}^{-1}$. In column 5 we give the local merger rate, which is the $z = 0$ value of the cosmic merger rate (see for instance Fig. 6 for model A) obtained as described in Sec. V, Eq. (9).

In Table 8 of Ref. [72], the Galactic rates obtained with different population synthesis codes, based on different assumptions on stellar/binary evolution, are compared. The values reported in that table range between 0.01 and 250 Myr^{-1} , and values that are considered as “realistic” range within 0.01 and 20 Myr^{-1} . If we compare these estimates with the Galactic merger rates given in column 4 of Table V, we see that our values are in the realistic range, except for the model F3, which we will discuss below.

We first consider models where we vary the common envelope parameter (models B1 and B5). This parameter does not affect the birth rate but controls the number of merging systems: in fact, a larger (smaller) CE parameter, such as in model B5 (B1), generates binaries which, at the end of the CE phase, are characterized by larger (smaller)

orbital separations and therefore longer (shorter) merger time scales. The resulting fraction of merging systems in model B5 is only 0.12% of the total (BH-BH) binaries, more than a factor 10 smaller than for the reference model A.

The adopted shape and velocity dispersion of the kick distribution affect both the birth and merger rates (see models C1, C2, C5, and C7). In the first two models, we assume a Paczyński distribution for kick velocities,

$$P(u)du = \frac{4}{\pi} \frac{du}{(1+u^2)^2}, \quad (14)$$

where $u = v/\sigma$ and the dispersion velocity σ is, respectively, 150 and 600 km s^{-1} for models C1 and C2. In models C5 and C7 we consider a Maxwellian distribution,

$$P(v)dv = \sqrt{\frac{2}{\pi}} v^2 e^{-[v^2/(2\sigma^2)]} \quad (15)$$

with $\sigma = 200$ and 600 km s^{-1} , respectively. For both distributions, the birth rate decreases with increasing σ . However, the fraction of formed binaries which coalesces increases slightly with σ . The first effect is a direct consequence of the disruption of the binary after the SN explosion (it is more likely that a strong kick disrupts the system). The increase of the merger rate with σ is due to the net effect of kicks on the orbit of systems which are not disrupted: while the semimajor axis is left mostly unchanged, the eccentricity is greatly enhanced, favoring the orbital decay due to GW emission. As a result, in model C2 the number of merging pairs is a factor 2 larger than in model A (3.4% of the total sample). In the extreme case of null kicks, such as in model C8, we find a birth rate which is a factor 2.3 larger than in model A. Yet, the corresponding merger rates are comparable in the two models.

TABLE V. In columns 3 and 4 we give the Galactic birth (BR)/merger rates (MR) for the different models, obtained by varying one key parameter (indicated in column 2) with respect to the reference model A (see text). In column 5 we give the local merger rate, which is the $z = 0$ value of the merger rate (see for instance Fig. 6 for model A) obtained as described in Sec. V, Eq. (9).

EXPLORATION OF THE PARAMETER SPACE				
Model	Modified parameter	Galactic (BH-BH) BR (Myr^{-1})	Galactic (BH-BH) MR (Myr^{-1})	Local (BH-BH) MR ($\text{Mpc}^{-3} \text{ Myr}^{-1}$)
A	Reference model	95	1.8	5.3×10^{-2}
B1	$\alpha_{\text{CE}}\lambda = 0.5$	95	16	2.9×10^{-1}
B5	$\alpha_{\text{CE}}\lambda = 4$	96	1.2×10^{-1}	3.3×10^{-3}
C1	Paczyński distribution ($\sigma = 150 \text{ km s}^{-1}$)	120	1.7	5.1×10^{-2}
C2	Paczyński distribution ($\sigma = 600 \text{ km s}^{-1}$)	71	2.4	6.6×10^{-2}
C5	Maxwellian distribution ($\sigma = 200 \text{ km s}^{-1}$)	88	1.8	5.3×10^{-2}
C7	Maxwellian distribution ($\sigma = 600 \text{ km s}^{-1}$)	53	3.2	8.8×10^{-2}
C8	No kick distribution	220	1.7	5.3×10^{-2}
F1	$m_{\text{thre, BH}} = 8.5M_{\odot}$	140	7.6	2.0×10^{-1}
F2	$m_{\text{thre, BH}} = 7.6M_{\odot}$	160	15	3.6×10^{-1}
F3	$m_{\text{thre, BH}} = 5.5M_{\odot}$	240	40	8.5×10^{-1}

Finally, we discuss the dependence on the core mass threshold for BH formation (models F1-F3). This parameter appears to be the most important one for the GWB. In fact, a reduction in $m_{\text{thre, BH}}$ from the reference value of

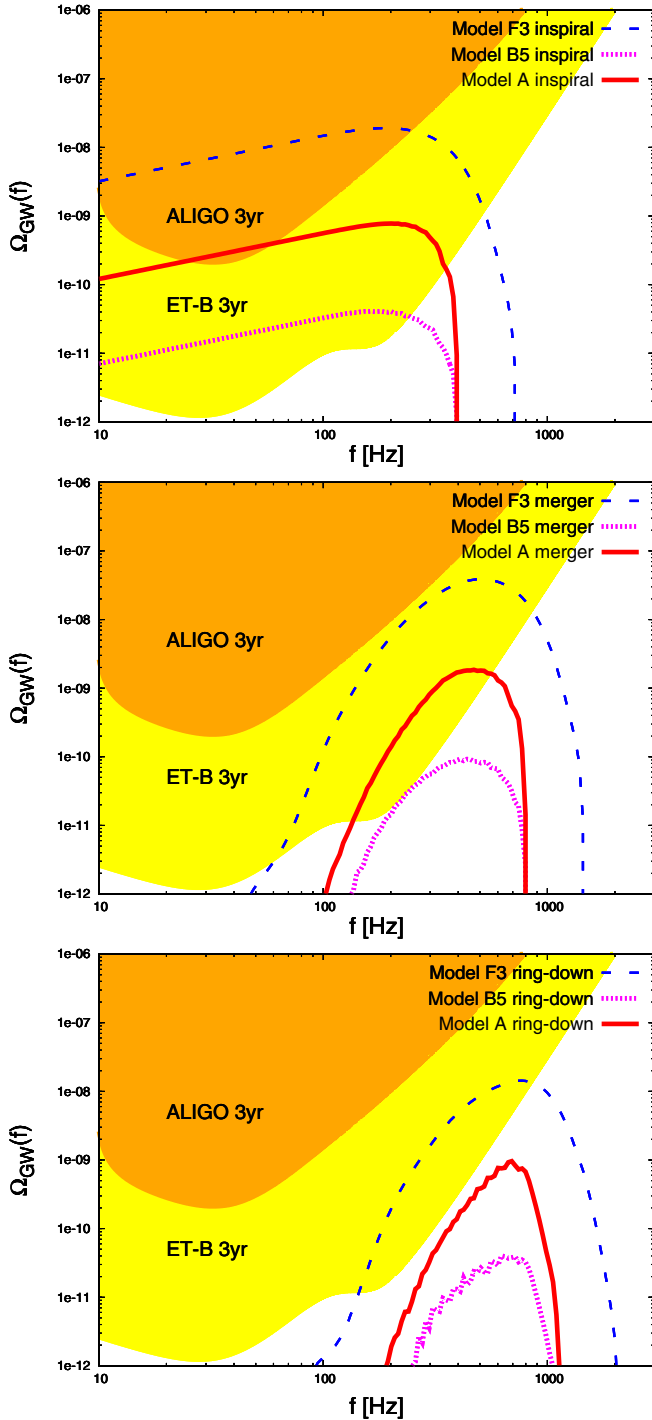


FIG. 8 (color online). Ω_{GW} generated during the inspiral (upper panel), merger (central panel), and ring-down (lower panel) phases in models F3 (dashed), B5 (dotted), and A (solid). In all panels, the two shaded regions indicate the foreseen sensitivities of ALIGO and ET-B assuming three years of integration.

$10M_{\odot}$ (model A) to $5.5M_{\odot}$ (model F3) leads to a birth rate which is a factor 2.5 larger. The amplification in the merger rate is even more dramatic, by more than a factor 20. This is due to the evolutionary path followed by massive stellar progenitors. In particular, a smaller $m_{\text{thre, BH}}$ allows the formation of BHs from lighter progenitor stars; the latter experience a smaller amount of mass loss (see Sec. II) forming close binary pairs characterized by shorter merger time scales.

The largest differences with respect to model A are found for models B5 and F3 which provide a sort of lower and upper limits to the (BH-BH) merger rate and GWB. In Fig. 9 we show the predicted redshift evolution of (BH-BH) merger rate in the two models as compared to model A. The upper limit labeled as “LIGO S5” shows the constraint derived in [73] from approximately two years of LIGO data (run S5) on the merger rate of systems with component masses in the range $19M_{\odot}$ – $28M_{\odot}$. Even the most optimistic model F3 predicts a local merger rate which is more than a factor 2 smaller than the upper limit inferred by the data analysis of the LIGO S5 run.

The longer (shorter) merger time scales predicted in model B5 (F3) lead to a reduction (amplification) of the overall cosmic merger rate, shifting it to smaller (larger) redshifts. This, in turn, affects the amplitude and frequency range of the resulting GWB spectra, as shown in Figs. 8 and 10.

In Fig. 8, we plot the contributions to Ω_{GW} generated during the inspiral (upper panel), merger (central panel), and ring-down (lower panel) phases comparing models F3, B5, and A. As expected, model F3 generates the strongest signals. It is also evident that the merger and ring-down signals in model F3 extend to lower frequencies with respect to models A and B5. This is due to the shorter merger time scales which allow a larger number of (BH-BH) binaries to reach the final coalescence at larger

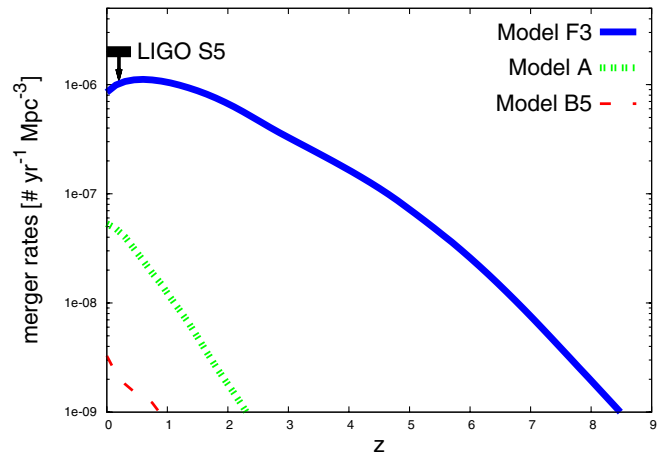


FIG. 9 (color online). Redshift evolution of (BH-BH) merger rates for models F3 (solid line), A (dotted line), and B5 (dashed line). The upper limit labeled “LIGO S5” shows the constraint recently derived in [73] (see text).

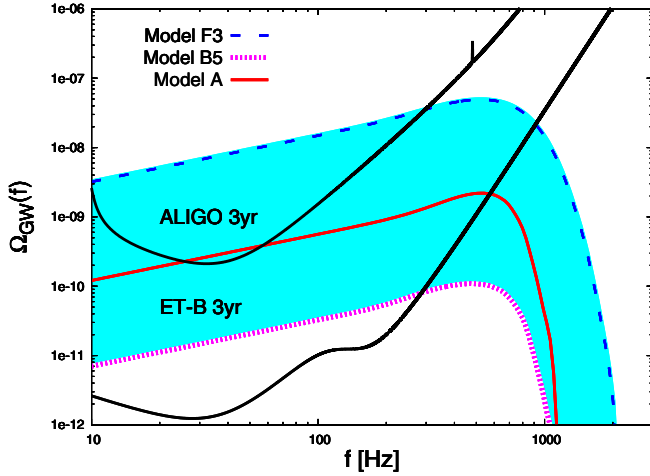


FIG. 10 (color online). The closure energy density, Ω_{GW} , for (BH-BH) binaries predicted by models F3 (dashed line) and B5 (dotted line) is compared to that of model A (solid line). The shaded region can be considered a measure of the uncertainty on Ω_{GW} . The two black solid lines indicate the foreseen sensitivities of ALIGO and ET-B assuming three years of integration.

redshifts (see Fig. 9), emitting signals contributing at smaller observational frequencies. Similarly, the differences among models A and B5 can be traced back to the merger time scales which, for models B5, confines (BH-BH) coalescence to redshifts $z < 1$. It is also interesting to note that, while models A and B5 show a similar behavior at the largest frequencies, model F3 systematically extends to larger frequencies. In fact, the smaller black hole masses predicted in model F3 (as a consequence of the smaller $m_{\text{thre, BH}}$) lead to larger f_{merge} , f_{ring} , and f_{cut} .

The shaded region in Fig. 10 illustrates the largest variations of the GWB among the models, and can be viewed as an indication of the uncertainty affecting its estimate. For the models we consider, the peak amplitude in the closure energy density ranges within $10^{-10} \leq \Omega_{\text{GW}} \leq 5 \times 10^{-8}$ at frequencies $470 \text{ Hz} \leq f \leq 510 \text{ Hz}$.

Table VI quantifies these differences in terms of the predicted signal-to-noise ratio. For the sake of comparison, we consider the same integration times and detector

configurations/orientations as in Table IV, which refer to model A. The major difference with respect to the data in Table IV is that, for model F3, ALIGO has a chance to probe the inspiral part of the GWB with an integration time of 1 yr and (S/N) larger than 10.

VII. DISCUSSION AND CONCLUSIONS

Many astrophysical processes which control the formation and evolution of (BH-BH) binaries, starting from their stellar progenitors, are still poorly understood. Of particular relevance in this respect are the amount of mass loss by massive stars, presupernova and supernova evolution, the effects of mass transfer among the two companion stars on the subsequent evolution of the system. In the present study, we have considered a reference model (A), which adopts a set of “standard” conservative assumptions, reproducing the observed properties of single Wolf-Rayet stars and double pulsars ([37] and references therein). Furthermore, we have explored a wide range of parameters on which our simulations depend (see Table I), to extract those that have the largest impact on the GWB, i.e. the common envelope parameter, the core mass threshold for BH formation and the kick velocity distribution. Varying these parameters, we identify two models, B5 and F3, which produce, respectively, the smallest and largest gravitational wave background.

When normalized to a Galactic star formation rate, the Galactic birth and merger rates computed for the considered models are in good agreement with the results of independent studies (see [72] and references therein, and the discussion in Sec. V).

To model the single source emission, we use the hybrid waveforms given in [14], which refer to nonspinning (BH-BH) binaries. This model has been improved in [74] with the inclusion of the effect of nonprecessing spins, and of a more accurate modeling of the nonspinning case. A comparison of the GWB obtained with the waveforms of [14] and of [74], for our reference model A, assuming the single spin parameter $\chi = 0$ (nonspinning case), shows no significant differences. Even assuming that all (BH-BH) binaries have $\chi = 0.85$ (which is the extreme case

TABLE VI. The (S/N) ratio for second and third generation detectors assuming different integration times and detector separation/orientation. These values have been computed considering separate contributions from the inspiral, merger, and ring-down phases for models F3 and B5. The numbers in square brackets refer to a nonoptimal orientation of the detectors (see the discussion in Sec. VI A).

(S/N)					
Case II [Case I]					
GWB	Model	ALIGO (1 yr)	ALIGO (3 yr)	ET-B (1 yr)	ET-B (3 yr)
Inspirals	F3	29 [10]	50 [19]	4720 [1770]	8176 [3065]
Inspirals	B5	6.4×10^{-2} [2.4×10^{-2}]	0.1 [4.1×10^{-2}]	10 [3.9]	18 [6.7]
Merger	F3	1.1 [1.3×10^{-2}]	1.9 [2.3×10^{-2}]	442 [165]	766 [287]
Merger	B5	3.0×10^{-3} [3.3×10^{-5}]	5.2×10^{-3} [5.6×10^{-5}]	1.2 [0.4]	2.1 [0.8]
Ring-down	F3	0.1 [7.0×10^{-4}]	0.2 [1.2×10^{-3}]	32 [12]	56 [21]
Ring-down	B5	3.3×10^{-4} [1.7×10^{-6}]	5.7×10^{-4} [2.9×10^{-6}]	8.2×10^{-2} [3.0×10^{-2}]	0.1 [5.3×10^{-2}]

considered in [74]), the GWB shows some difference only above ~ 1 kHz, in a region where even ET could not detect it. This evidence has been reported also in [7]. In [74] it is stated that the nonprecessing waveforms are effectual in capturing also precessing binaries, especially in the comparable-mass regime. Since most of our systems have $q < 1.1$ (see Fig. 4) the inclusion of spin precession is not expected to significantly change our results.

As mentioned in the Introduction, the same waveforms have been recently used by [7] to estimate the gravitational wave background. This study adopts a fixed merger time distribution function, an average chirp mass to describe all the (BH-BH) systems, and normalize the binary merger rate to a “local” merger rate (LMR); the latter quantity is computed multiplying the Galactic merger rates predicted by population synthesis models [50], by the average number density of Milky Way-type galaxies in the Local Universe (assumed to be 0.01 Mpc^{-3}). Thus, there are many differences between this study and the present one. As explained in Sec. V, we do not normalize the cosmic merger rate to a “rescaled” Galactic rate; indeed, we compute it integrating the star formation history over the birth and merger time distribution functions predicted by each SeBa run. The resulting local rates, at $z = 0$, are shown in column 5 of Table V, and are a factor 2–3 (depending on the model) larger than what would be obtained from the corresponding Galactic merger rate (column 4), applying the procedure of [7]. In fact, due to their long merger times, a large fraction of the (BH-BH) progenitors form at $z \geq 1$ close to the peak of the cosmic star formation rate. In addition, our analysis shows that there exist correlations between the distributions of merger times, hence the merger rate, and the distribution of the chirp masses (see Fig. 3). Thus, the points of the detectable parameter space explored by [7], identified by an average chirp mass and a LMR, do not have the same probability to represent a physical model. Our study shows that variations of key physical parameters produce *correlated* effects on the merger time and chirp mass distributions and, as a consequence, on the amplitude and the spectral energy distribution of the gravitational wave background (see, for instance, the discussion on model F3 in Sec. VIB). These properties can be appreciated only using the full rich information provided by population synthesis models.

Our main results can be summarized as follows:

- (i) For the reference model A, the sample of simulated (BH-BH) binaries is characterized by BH masses which vary between $\sim 6M_{\odot}$ and $\sim 20M_{\odot}$, with the largest concentration in the range $[10\text{--}15]M_{\odot}$. The formation of (BH-BH) binaries from their stellar progenitors is characterized by relatively short time scales, $\sim 3.5\text{--}6$ Myr and by a wide interval of semimajor axes ranging between $\sim 10R_{\odot}$ to several thousands of R_{\odot} . Only 2% of the formed (BH-BH)

binaries are able to merge within the Hubble time. These systems are characterized by semimajor axes $< 20R_{\odot}$, and black hole mass ratios close to 1. The majority of these systems (70%) have merger time scales ≥ 6 Gyr. As a result, (BH-BH) Galactic birth and merger rates are, respectively, $9.5 \times 10^{-5} \text{ yr}^{-1}$ and $1.8 \times 10^{-6} \text{ yr}^{-1}$. On cosmic scales, the (BH-BH) birth rate closely follows the shape of the cosmic star formation rate (although with a significantly reduced amplitude); conversely, the merger rate shows a significant time delay, and it is negligible beyond $z \sim 2$. The above conclusions mostly depend on the adopted common envelope parameter and core mass threshold for BH formation ($\alpha_{\text{CE}}\lambda = 2$ and $m_{\text{thre, BH}} = 10M_{\odot}$ in model A).

- (ii) An increase of the CE parameter to $\alpha_{\text{CE}}\lambda = 4$, as in model B5, generates (BH-BH) binaries with larger orbital separation, reducing the (BH-BH) merger rate (by a factor of 10 for the Galactic value) and confining the mergers to occur at $z < 1$. Conversely, a reduction in $m_{\text{thre, BH}}$ to $5.5M_{\odot}$, as in model F3, leads to an increase of the Galactic merger rate by more than a factor 20. Variations in these physical parameters also affect the distribution of black hole masses.
- (iii) The GWB is characterized by a peak amplitude in the range $10^{-10} \leq \Omega_{\text{GW}} \leq 5 \times 10^{-8}$ at frequencies $470 \text{ Hz} \leq f \leq 510 \text{ Hz}$, when the uncertainties on some key physical parameters are considered (see Fig. 10).
- (iv) Advanced LIGO/Virgo have a chance to detect the GWB from the inspiral only in model F3, which predicts the highest merger rate; third generation detectors like ET, would detect the inspiral GWB with high (S/N) for models spanning the region from model A ($(S/N) \geq 6$) to model F3 ($(S/N) \geq 165$), with 1 yr integration.
- (v) The merger contribution to the GWB could be detected only by ET. From Fig. 8 and Tables IV and VI, we see that ET-B could detect this contribution for models spanning the region from model A ($(S/N) \geq 6$) to model F3 ($(S/N) \geq 165$), with 1 yr integration.
- (vi) The ring-down contribution could be detected by ET-B with 1 yr integration only for model F3 ($(S/N) \geq 12$).

We find that the amplitude of the GWB is very sensitive to the adopted core mass threshold for BH formation (models F1 to F3). This opens up the possibility to constrain the uncertain physics related to the final stages of the evolution of massive stars using observational constraints on the associated gravitational wave emission.

Finally, we would like to mention that, according to a recent study [50], (BH-BH) binaries formed in a

low-metallicity environment are characterized by higher coalescence rates and chirp masses than their solar metallicity counterparts. Indeed, at subsolar metallicities stars are more compact (smaller radii), experience reduced mass loss (larger masses), and BHs can form by direct collapse of the progenitor (no kick due to the SN explosion). These changes result in an increase of the galactic and local merger rate. Metallicity-dependent evolutionary tracks are currently being implemented in SeBa [75], and their effects on the gravitational wave background will be considered in a future study.

ACKNOWLEDGMENTS

We thank Tania Regimbau, Xing-Jiang Zhu, and Pablo Rosado for fruitful comments which enabled us to improve this paper. We also acknowledge Francesco Pannarale for his careful reading of the manuscript. Stefania Marassi thanks Francesco Simula for technical support. This work was partly supported by the Netherlands Research Council NWO (via Grants No. 643.200.503, No. 639.073.803, and No. 614.061.608) and the Netherlands Research School for Astronomy (NOVA).

-
- [1] R. Schneider, V. Ferrari, S. Matarrese, and S.F. Portegies Zwart, *Mon. Not. R. Astron. Soc.* **324**, 797 (2001).
- [2] V.B. Ignatiev, A.G. Kuranov, K.A. Postnov, and M.E. Prokhorov, *Mon. Not. R. Astron. Soc.* **327**, 531 (2001).
- [3] G. Nelemans, L.R. Yungelson, and S.F. Portegies Zwart, *Astron. Astrophys.* **375**, 890 (2001).
- [4] T. Regimbau and J.A. de Freitas Pacheco, *Astrophys. J.* **642**, 455 (2006).
- [5] T. Regimbau and B. Chauvineau, *Classical Quantum Gravity* **24**, S627 (2007).
- [6] K. Belczynski, M. Benacquista, and T. Bulik, *Astrophys. J.* **725**, 816 (2010).
- [7] X.J. Zhu, E. Howell, T. Regimbau, D. Blair, and Z.H. Zhu, *Astrophys. J.* **739**, 86 (2011).
- [8] T. Regimbau, *Res. Astron. Astrophys.* **11**, 369 (2011).
- [9] C. Cutler and D. Holz, *Phys. Rev. D* **80**, 104009 (2009).
- [10] S.R. Taylor, J.R. Gair, and I. Mandel, arXiv:1108.5161.
- [11] B. Allen and J.D. Romano, *Phys. Rev. D* **59**, 102001 (1999).
- [12] M. Maggiore, *Phys. Rep.* **331**, 283 (2000).
- [13] T. Regimbau and V. Mandic, *Classical Quantum Gravity* **25**, 184018 (2008).
- [14] P. Ajith, *Classical Quantum Gravity* **25**, 114033 (2008).
- [15] L.R. Yungelson, J. Lasota, G. Nelemans, G. Dubus, E.P.J. van den Heuvel, J. Dewi, and S.F. Portegies Zwart, *Astron. Astrophys.* **454**, 559 (2006).
- [16] S. Marassi, R. Schneider, and V. Ferrari, *Mon. Not. R. Astron. Soc.* **398**, 293 (2009).
- [17] S. Marassi, R. Ciolfi, R. Schneider, L. Stella, and V. Ferrari, *Mon. Not. R. Astron. Soc.* **411**, 2549 (2011).
- [18] L. Tornatore, A. Ferrara, and R. Schneider, *Mon. Not. R. Astron. Soc.* **382**, 945 (2007).
- [19] R.J. Bouwens *et al.*, *Astrophys. J.* **709**, L133 (2010).
- [20] S.F. Portegies Zwart and S.L.W. McMillan, *Astrophys. J.* **528**, L17 (2000).
- [21] R.M. O’Leary, R. O’Shaughnessy, and F.A. Rasio, *Phys. Rev. D* **76**, 061504 (2007).
- [22] A. Sadowski, K. Belczynski, T. Bulik, N. Ivanova, F.A. Rasio, and R. O’Shaughnessy, *Astrophys. J.* **676**, 1162 (2008).
- [23] M.C. Miller and V. Lauburg, *Astrophys. J.* **692**, 917 (2009).
- [24] S.F. Portegies Zwart and F. Verbunt, *Astron. Astrophys.* **309**, 179 (1996).
- [25] S.F. Portegies Zwart and L.R. Yungelson, *Astron. Astrophys.* **332**, 173 (1998).
- [26] G. Nelemans, L.R. Yungelson, S.F. Portegies Zwart, and F. Verbunt, *Astron. Astrophys.* **365**, 491 (2001).
- [27] C.L. Fryer and V. Kalogera, *Astrophys. J.* **554**, 548 (2001).
- [28] S. Toonen, G. Nelemans, and S.F. Portegies Zwart, *AIP Conf. Proc.* **1314**, 266 (2010).
- [29] R.F. Webbink, *Astrophys. J.* **277**, 355 (1984).
- [30] M. de Kool, E.P.J. van den Heuvel, and E. Pylyser, *Astron. Astrophys.* **183**, 47 (1987).
- [31] P. Podsiadlowski, S. Rappaport, and Z. Han, *Mon. Not. R. Astron. Soc.* **341**, 385 (2003).
- [32] T.M. Tauris and J.D.M. Dewi, *Astron. Astrophys.* **369**, 170 (2001).
- [33] G. Nelemans and C.A. Tout, *Mon. Not. R. Astron. Soc.* **356**, 753 (2005).
- [34] P.D. Kiel and J.R. Hurley, *Mon. Not. R. Astron. Soc.* **369**, 1152 (2006).
- [35] L.R. Yungelson and J. Lasota, *Astron. Astrophys.* **488**, 257 (2008).
- [36] C.J. Deloye and R.E. Taam, *Astrophys. J.* **719**, L28 (2010).
- [37] K.A. Postnov and L.R. Yungelson, *Living Rev. Relativity* **9**, 6 (2006).
- [38] M. Burgay, N. D’Amico, A. Possenti, R.N. Manchester, A.G. Lyne, B.C. Joshi, M.A. McLaughlin, M. Kramer, J.M. Sarkissian, F. Camilo, V. Kalogera, C. Kim, and D.R. Lorimer, *Nature (London)* **426**, 531 (2003).
- [39] V. Kalogera, C. Kim, D.R. Lorimer, M. Burgay, N. D’Amico, A. Possenti, R.N. Manchester, A.G. Lyne, B.C. Joshi, M.A. McLaughlin, M. Kramer, J.M. Sarkissian, and F. Camilo, *Astrophys. J.* **601**, L179 (2004).
- [40] P.G. Jonker and G. Nelemans, *Mon. Not. R. Astron. Soc.* **354**, 355 (2004).
- [41] B. Willems, M. Henninger, T. Levin, N. Ivanova, V. Kalogera, K. McGhee, F.X. Timmes, and C.L. Fryer, *Astrophys. J.* **625**, 324 (2005).
- [42] A. Gualandris, M. Colpi, S. Portegies Zwart, and A. Possenti, *Astrophys. J.* **618**, 845 (2005).
- [43] B. Paczynski, *Astrophys. J.* **348**, 485 (1990).
- [44] J.W. Hartman, *Astron. Astrophys.* **322**, 127 (1997).

- [45] G. Nelemans and E.P.J. van den Heuvel, *Astron. Astrophys.* **376**, 950 (2001).
- [46] T. Nugis and H.J.G.L.M. Lamers, *Astron. Astrophys.* **360**, 227 (2000).
- [47] H. A. Abt, *Annu. Rev. Astron. Astrophys.* **21**, 343 (1983).
- [48] A. Duquennoy and M. Mayor, *Astron. Astrophys.* **248**, 485 (1991).
- [49] S. F. Portegies Zwart, F. Verbunt, and E. Ergma, *Astron. Astrophys.* **321**, 207 (1997).
- [50] K. Belczynski, M. Dominik, T. Bulik, R. O’Shaughnessy, C. Fryer, and D. E. Holz, *Astrophys. J.* **715**, L138 (2010).
- [51] C. L. Fryer, A. Heger, and N. Langer, *Astrophys. J.* **578**, 335 (2002).
- [52] W. Zhang, S. E. Woosley, and A. Heger, *Astrophys. J.* **679**, 639 (2008).
- [53] We adopt a Λ CDM cosmological model with parameters $\Omega_M = 0.26$, $\Omega_\Lambda = 0.74$, $H_0 = 73$ km/Mpc/s, $\Omega_B = 0.041$.
- [54] I. Mandel and R. O’Shaughnessy, *Classical Quantum Gravity* **27**, 114007 (2010).
- [55] F. Ozel, D. Psaltis, R. Narayan, and J. E. McClintock, *Astrophys. J.* **725**, 1918 (2010).
- [56] L. P. Grishchuk, V. M. Lipunov, K. A. Postnov, M. E. Prokhorov, and B. S. Sathyaprakash, *Phys. Usp.* **44**, 1 (2001).
- [57] P. C. Peters, *Phys. Rev.* **136**, B1224 (1964).
- [58] P. C. Peters and J. Mathews, *Phys. Rev.* **131**, 435 (1963).
- [59] R. Schneider, A. Ferrara, P. Natarajan, and K. Omukai, *Astrophys. J.* **571**, 30 (2002).
- [60] R. Schneider, A. Ferrara, R. Salvaterra, K. Omukai, and V. Bromm, *Nature (London)* **422**, 869 (2003).
- [61] K. Omukai, T. Tsuribe, R. Schneider, and A. Ferrara, *Astrophys. J.* **626**, 627 (2005).
- [62] E. Cappellaro, R. Evans, and M. Turatto, *Astron. Astrophys.* **351**, 459 (1999).
- [63] R. Voss and T. M. Tauris, *Mon. Not. R. Astron. Soc.* **342**, 1169 (2003).
- [64] The ALIGO sensitivity curve is described in the public LIGO document ligo-t0900288 (<https://dcc.ligo.org/public/0002/T0900288/002/AdvLIGOnoisecurve.pdf>).
- [65] E. Howell, T. Regimbau, A. Corsi, D. Coward, and R. Burman, *Mon. Not. R. Astron. Soc.* **410**, 2123 (2011).
- [66] S. Hild, S. Chelkowski, A. Freise, J. Franc, N. Morgado, R. Flaminio, and R. DeSalvo, *Classical Quantum Gravity* **27**, 015003 (2010).
- [67] For ET this condition is not satisfied, but new techniques to remove instrumental correlation are under development [65].
- [68] T. Regimbau and S. A. Hughes, *Phys. Rev. D* **79**, 062002 (2009).
- [69] S. Drasco and E. E. Flanagan, *Phys. Rev. D* **67**, 082003 (2003).
- [70] P. A. Rosado, *Phys. Rev. D* **84**, 084004 (2011).
- [71] B. Allen, J. D. Creighton, É. É. Flanagan, and J. D. Romano, *Phys. Rev. D* **65**, 122002 (2002).
- [72] J. Abadie *et al.*, *Classical Quantum Gravity* **27**, 173001 (2010).
- [73] J. Abadie *et al.*, *Phys. Rev. D* **83**, 122005 (2011).
- [74] P. Ajith *et al.*, *Phys. Rev. Lett.* **106**, 241101 (2011).
- [75] S. Toonen *et al.* (to be published).